AGU PUBLICATIONS

JGR

Journal of Geophysical Research: Space Physics

RESEARCH ARTICLE
10.1002/2013JA019706

This article is a companion to *Richard et al.* [2015], doi:10.1002/2014JA020343.

Key Points:
- Electron and ion density discrepancies are not due to primary ion overproduction
- Production rate profiles for ionization products of N_2 and CH_4 were created
- Empirical N_2^+ and CH_4^+ production profiles have been generated

Correspondence to:
T. E. Cravens,
cravens@ku.edu

Citation:
Richard, M. S., et al. (2015), An empirical approach to modeling ion production rates in Titan's ionosphere I: Ion production rates on the dayside and globally, *J. Geophys. Res. Space Physics*, *120*, 1264–1280, doi:10.1002/2013JA019706.

Received 12 DEC 2013
Accepted 12 JUL 2014
Accepted article online 7 SEP 2014
Published online 3 FEB 2015

An empirical approach to modeling ion production rates in Titan's ionosphere I: Ion production rates on the dayside and globally

M. S. Richard[1,2], T. E. Cravens[1], C. Wylie[1], D. Webb[1], Q. Chediak[1], R. Perryman[3], K. Mandt[3], J. Westlake[4], J. H. Waite Jr.[3], I. Robertson[1], B. A. Magee[3], and N. J. T. Edberg[5]

[1]Department of Physics and Astronomy, University of Kansas, Lawrence, Kansas, USA, [2]Department of Physics and Astronomy, Benedictine College, Atchison, Kansas, USA, [3]Space Science and Engineering Division, Southwest Research Institute, San Antonio, Texas, USA, [4]Johns Hopkins University Applied Physics Laboratory, Laurel, Maryland, USA, [5]Swedish Institute of Space Physics, Uppsala, Sweden

Abstract Titan's ionosphere is created when solar photons, energetic magnetospheric electrons or ions, and cosmic rays ionize the neutral atmosphere. Electron densities generated by current theoretical models are much larger than densities measured by instruments on board the Cassini orbiter. This model density overabundance must result either from overproduction or from insufficient loss of ions. This is the first of two papers that examines ion production rates in Titan's ionosphere, for the dayside and nightside ionosphere, respectively. The first (current) paper focuses on dayside ion production rates which are computed using solar ionization sources (photoionization and electron impact ionization by photoelectrons) between 1000 and 1400 km. In addition to theoretical ion production rates, empirical ion production rates are derived from CH_4, CH_3^+, and CH_4^+ densities measured by the INMS (Ion Neutral Mass Spectrometer) for many Titan passes. The modeled and empirical production rate profiles from measured densities of N_2^+ and CH_4^+ are found to be in good agreement (to within 20%) for solar zenith angles between 15 and 90°. This suggests that the overabundance of electrons in theoretical models of Titan's dayside ionosphere is not due to overproduction but to insufficient ion losses.

1. Introduction

Titan's ionosphere was first detected via radio occultation data generated from Voyager 1 [*Bird et al.*, 1997] and later by the Cassini Radio Science Subsystem [*Kliore et al.*, 2008]. The first in situ measurements of the ionosphere were made by the Cassini spacecraft [*Cravens et al.*, 2009a, 2009b], showing electron and total ion densities peaking between 900 and 1200 km as expected from models [*Wahlund et al.*, 2005; *Young et al.*, 2005; *Keller et al.*, 1992; *Gan et al.*, 1992; *Cravens et al.*, 2004, 2005, 2008; *Galand et al.*, 1999; *Banaskiewicz et al.*, 2000; *Molina-Cuberos et al.*, 2001; *Lilensten et al.*, 2005a, 2005b; *Agren et al.*, 2007; *Kliore et al.*, 2008; *Edberg et al.*, 2010, 2013a]. Negative ions have also been detected in Titan's ionosphere and could have significant impacts on the ion chemistry [*Coates et al.*, 2007; *Ågren et al.*, 2012; *Shebanits et al.*, 2013]. The ionosphere results from the ionization of Titan's neutral atmosphere, which is composed of nitrogen, methane, hydrogen, and minor hydrocarbon and nitriles [*Waite et al.*, 2004, 2005, 2007; *Vuitton et al.*, 2006, 2007; *Magee et al.*, 2009].

Photoionization is the main source of Titan's ionosphere between 900 and 1400 km on the dayside of Titan [cf. *Cravens et al.*, 2004, 2005, 2009b; *Robertson et al.*, 2009; *Gronoff et al.*, 2009a; *Galand et al.*, 2010; *Lavvas et al.*, 2011; *Kliore et al.*, 2011; *Luhmann et al.*, 2012; *Mandt et al.*, 2012; *Vigren et al.*, 2013]. Solar photons deposit their energy in the atmosphere due to photoionization or excitation of neutrals. *Edberg et al.* [2013a] have shown that photoionization rates and electron densities strongly correlate with the solar cycle variation when considering flybys up to T88.

Electron impact ionization of the neutral atmosphere is responsible for the bulk of ion production on the nightside of Titan above 1000 km and for a substantial portion of the energy deposition of the region below 1000 km on the dayside and nightside [cf. *Agren et al.*, 2007; *Cravens et al.*, 2006; *Cravens et al.*, 2009a, 2009b; *Robertson et al.*, 2009; *Gronoff et al.*, 2009b]. On the dayside, however, electron impact ionization accounts for only 5–10% of the ion production [*Robertson et al.*, 2009; *Lavvas et al.*, 2011; *Vigren et al.*, 2013]., *Edberg et al.*

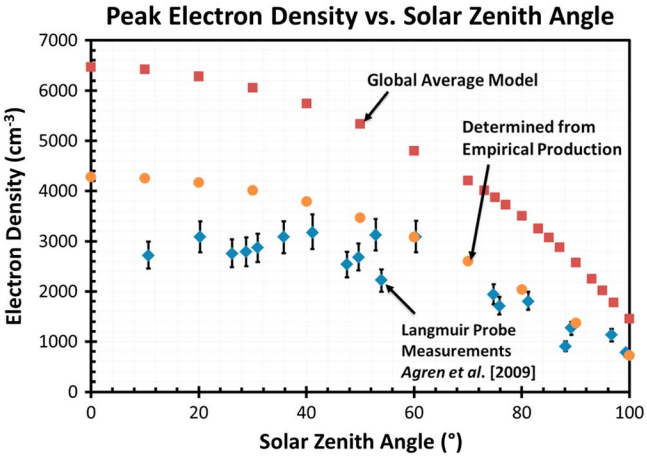

Figure 1. Peak electron density versus solar zenith angle at Titan. Measurements by the Langmuir probe (RPWS/LP) [*Ågren et al.*, 2009] are the filled blue diamonds. The red squares are peak electron densities from the current paper's global average model (and baseline chemistry). Orange circles indicate electron densities obtained for the global average production and an effective electron-ion recombination coefficient.

[2013b] reported the highest RPWS/LP (Radio Plasma Wave Science/Langmuir Probe) electron density measurements to date recorded during the T85 flyby which are believed to be the result of extreme particle impact ionization.

Recently, *Lavvas et al.* [2011] and *Mandt et al.* [2012] have studied the impact of higher-resolution photoabsorption cross sections of *Liang et al.* [2007] on CH_4^+ production, and they have found that this improves agreement between measured and modeled CH_4^+ densities. Lavvas et al. computed ion production rates using the magnetospheric superthermal electron flux and solar photon flux for the T40 flyby of Titan for a radial magnetic field line and a solar zenith angle of 60°. The model of Lavvas et al. shows that ionization from solar sources dominates near 1000 km while the contribution from electron impact ionization caused by superthermal electrons dominates between 700 and 900 km.

Models of Titan's atmosphere featuring complex hydrocarbon and nitrile neutral-ion chemistry have been created pre- and post-Cassini to calculate ionospheric densities [*Keller et al.*, 1992, 1998; *Krasnopolsky*, 2009; *Lavvas et al.*, 2008a, 2008b; *Robertson et al.*, 2009; *Wilson and Atreya*, 2004; *Vuitton et al.*, 2006, 2007; *De la Haye et al.*, 2008]. Ion (most notably $HCNH^+$) and electron densities produced by current models are higher than the measurements recorded by the Cassini Ion–Neutral Mass Spectrometer (INMS) [*Kasprzak et al.*, 1996] aboard Cassini [e.g., *Robertson et al.*, 2009; *Galand et al.*, 2010; *Westlake et al.*, 2012; *Mandt et al.*, 2012; *Vigren et al.*, 2013].

In the present study, we use photoionization and two-stream codes [*Nagy and Banks*, 1970; *Gan et al.*, 1992; *Roboz and Nagy*, 1994; cf. *Schunk and Nagy*, 2009; *Cravens et al.*, 2009a; *Snowden et al.*, 2013] with draped magnetic field lines in conjunction with a photochemical model to determine ion densities. The densities produced by this model also exhibit the aforementioned problem as shown in Figure 1 where it is evident that the modeled electron densities at the peak are higher than the densities observed by the RPWS-Langmuir Probe as reported by *Ågren et al.* [2009].

Two possible reasons for the discrepancy between the modeled electron densities and the peak electron densities measured by the RPWS/LP (Figure 1) have been considered in the recent literature: (1) overproduction of primary ions or (2) insufficient chemical loss processes (i.e., the effective electron-ion dissociative recombination rate is not large enough to adequately remove electrons and ions, missing ion-neutral chemical pathways, or the impact of negative ion chemistry). In order to address the possible overproduction issue, the current paper reexamines ion production on the dayside. As part of this effort, we derive empirical production rates from INMS measurements of ion and neutral densities for all available Titan flybys and use these to determine an effective dissociative electron recombination rate. These empirical rates can be compared with theoretical model ion production rates, allowing one to check for possibly missing ionization processes or providing ion production rates when input information the models need (e.g., solar fluxes) might be missing. By comparing empirical production rates to modeled production rates of the primary ion species (N_2^+ and CH_4^+), we will demonstrate that the majority of the ion overabundance is a result of insufficient loss processes.

2. Methodology

The methodology employed follows from the methods of *Gan et al.* [1992], *Keller et al.* [1992], *Cravens et al.* [2005], *Robertson et al.* [2009], and *Richard et al.* [2011]. This model calculates primary population of ions from photoionization and ionization from electron impact ionization of neutrals using the flux of solar photons.

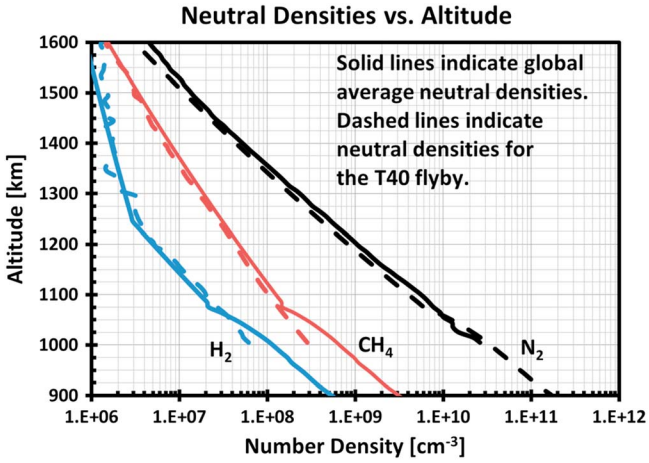

Figure 2. Neutral densities of major species for the T40 flyby of Titan measured by INMS (dashed lines) and global average neutral densities based on 40 flybys of Titan reported by *Magee et al.* [2009] (solid lines).

The chemistry in the theoretical model additionally follows from *Keller et al.* [1998] and *Westlake et al.* [2011, 2012]. Only a brief description of the theoretical model will be given, and the reader is referred to the above papers. The empirical ion production rate methodology will be described in more detail.

2.1. Neutral and Ion Densities

For the major neutral species (N_2, CH_4, and H_2) density measurements made by the INMS instrument during ingress of each flyby were used (Figure 2). INMS measurements for egress have been shown to be less accurate due to potential sticking effects in the antechamber of the closed source of the instrument [*Magee et al.*, 2009; *Cui et al.*, 2009; *Westlake et al.*, 2011, 2012]. Nonetheless, for some of our empirical production rates, we have used egress CH_4 measurements.

The absolute neutral and ion densities obtained from INMS measurements depend on the instrument calibration, which is a source of systematic error for any instrument. The INMS calibration was considered by *Mandt et al.* [2012], and we used the ion densities consistent with this paper. The calibration efforts are continuing (J. H. Waite et al., manuscript in preparation, 2014), and there is some indication that the INMS closed source neutral density calibration factor might be closer to 2.5 than to the factor of 3.15 adopted in the current paper, and the factor for open source ion measurements might be a factor of 1.5 higher than what we used (from the Mandt et al. paper). The main products of our paper are empirical ion production rates for the major species N_2 and CH_4, and these production rates are calculated from the product of neutral and ion densities. The calculated empirical production rates could thus be higher than those originally calculated for this paper by about 20%. However, 20% is within the majority of the data's statistical error bars, and the conclusions of the paper are not affected.

For the remaining 35 "minor" neutral species, altitude profiles of the mixing ratios from *Krasnopolsky* [2009] (or *Lavvas et al.* [2011] for the case of CH_2NH) were anchored to global mixing ratios reported by *Magee et al.* [2009], *Cui et al.* [2009], and *Robertson et al.* [2009] or fit as a model parameter (see Table 1 for the mixing ratio of the neutral species). In addition to specific Titan passes, a global average model of the neutral atmosphere was developed using the densities of N_2, CH_4, and H_2 measured by INMS and presented by *Magee et al.* [2009] for 40 Titan flybys. The basic fitting equation used by *Keller et al.* [1992] was applied, and the factor of 3.15 was included (Figure 2). We use this atmosphere for our calculations of global ion production rates.

2.2. Photoionization

Photoionization rates are calculated as a function of altitude and solar zenith angle for photons over a range of energies. Chapman functions taking into account spherical geometry have been employed to calculate the neutral column densities [*Cravens et al.*, 2004, 2009a], which have been calculated by *Smith and Smith* [1972] [cf. *Schunk and Nagy*, 2009].

The solar photon flux versus wavelength is taken from both the solar extreme ultraviolet flux model for aeronomic calculations (EUVAC) [*Richards et al.*, 1994] and the Solar Irradiance Platform (SIP, formerly SOLAR2000) [*Tobiska et al.*, 2000; *Tobiska*, 2007] models, which are based on measurements made near Earth. The fluxes were appropriately reduced to account for Titan's distance from the Sun. In both models, for wavelengths below 3.0 nm we use 0.1 nm bins and scale YOHKOH observations [*Acton et al.*, 1999; *Cravens et al.*, 2006] such that the total flux matches the EUVAC and SIP fluxes in the overlapping

Table 1. Mixing Ratios for the Minor Neutral Species

Neutral	Mixing Ratio	Anchor Point (km)	Source	Notes
N	6.560E−05	1100	*Robertson et al.* [2009]	
NH	5.920E−04	1100	*Robertson et al.* [2009]	
C_2H_2	3.420E−04	1050	*Magee et al.* [2009]	
C_2H_4	3.910E−04	1050	*Magee et al.* [2009]	
HCN	2.440E−04	1050	*Magee et al.* [2009]	
C_2H_6	4.570E−05	1050	*Magee et al.* [2009]	
H	9.790E−04	1100	*Robertson et al.* [2009]	
C_3HN	1.480E−06	1050	*Magee et al.* [2009]	
C_3H_4	9.200E−06	1050	*Magee et al.* [2009]	
H_2O	2.79E−06	1025	*Cui et al.* [2009]	
C_3H_8	2.870E−06	1050	*Magee et al.* [2009]	
C_4H_2	5.550E−06	1050	*Magee et al.* [2009]	
CO	7.680E−06	1100	*Robertson et al.* [2009]	
C_3H_6	2.330E−06	1050	*Magee et al.* [2009]	
C_2N_2	2.140E−06	1050	*Magee et al.* [2009]	
C_3H_2	4.320E−05	1100	*Robertson et al.* [2009]	
C_4N_2	2.250E−05	1100	*Robertson et al.* [2009]	
CH_3	2.609E−03	1100	*Robertson et al.* [2009]	
NH_3	4.220E−05	1025	*Cui et al.* [2009]	
O	0.0E + 00	1100	*Robertson et al.* [2009]	
CH_2NH	1.020E−04	1100	*Robertson et al.* [2009]	Profile from *Lavvas et al.* [2011]
CH_3CN	1.510E−06	1025	*Cui et al.* [2009]	
C_2H_3CN	3.460E−07	1050	*Magee et al.* [2009]	
C_2H_5CN	1.540E−07	1050	*Magee et al.* [2009]	
CH_3NH_2	1.0E−08	1100	*Robertson et al.* [2009]	
C_6H_6	2.480E−06	1050	*Magee et al.* [2009]	
C_6H_2	8.0E−07	1100	*Robertson et al.* [2009]	
C_7H_4	3.0E−07	1100	*Robertson et al.* [2009]	
C_7H_8	2.510E−08	1050	*Magee et al.* [2009]	
C_8H_2	2.0E−07	1100	*Robertson et al.* [2009]	
C_4H_3N	4.0E−06	1100	*Robertson et al.* [2009]	
HC_5N	1.0E−06	1100	*Robertson et al.* [2009]	
C_5H_5N	4.0E−07	1100	*Robertson et al.* [2009]	
C_6H_3N	3.0E−07	1100	*Robertson et al.* [2009]	Profile of C_5H_5N
C_6H_7N	1.0E−07	1100	*Robertson et al.* [2009]	Profile of C_5H_5N

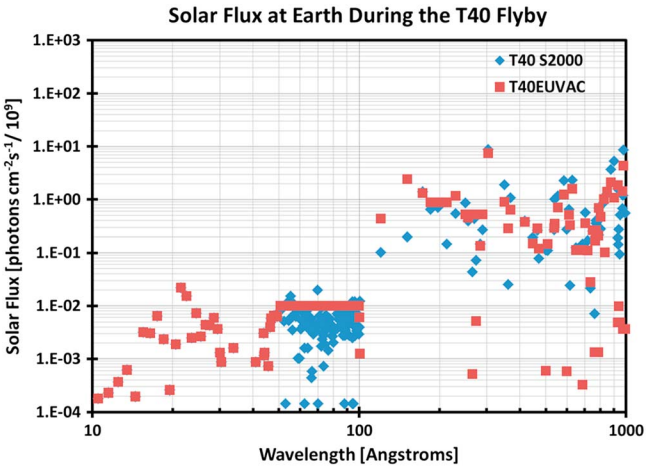

Figure 3. Flux of solar photons per bin at Earth in solar flux units (flux $cm^{-2}\,s^{-1}/10^9$) during the T40 flyby of Titan. Blue diamonds denote values produced by the SIP model [*Tobiska et al.*, 2000; *Tobiska*, 2007], and red squares are fluxes from the EUVAC model [*Richards et al.*, 1994]. The $F_{10.7}$ index is 79.7.

wavelength intervals. Figure 3 shows the solar photon flux at Earth for both models for the T40 flyby, taken during deep solar minimum.

Photoabsorption and photoionization cross sections for the two major neutral species (N_2 and CH_4) are also needed for the photoionization code. Cross sections for N_2 follow the work done by *Gan* [1991] and are used to compute N_2^+ and N^+ ion production and photoelectron production. This photoelectron population is then used as input into the two-stream electron code, where electron impact ionization rates are calculated. In this model, photoionization and photoabsorption cross sections from the works of *Gallagher et al.* [1988], *Solomon et al.* [1988], *Langhoff et al.* [1981], *Banks and*

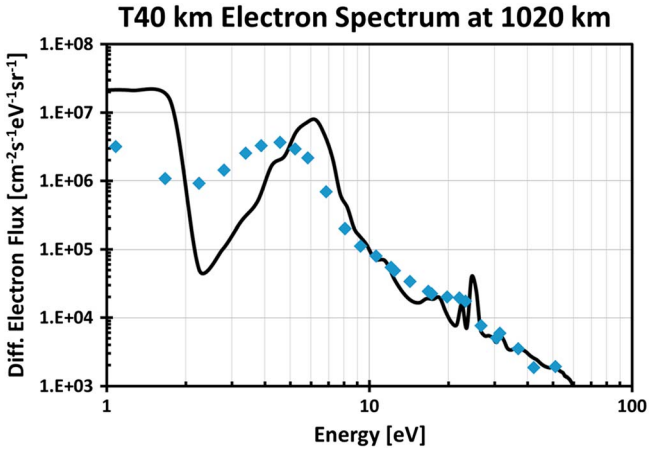

Figure 4. Electron spectrum observed by CAPS-ELS during the T40 of Titan assuming a spacecraft potential of −0.5 eV as reported by *Lavvas et al*. [2011] (blue diamonds) compared to the electron spectrum generated in our model (black line).

Kockarts [1973], and *Denne* [1970] are used as well as the N^+/N_2 photofragmentation cross section derived from data collected by *Wight et al*. [1976] and presented by *Gallagher et al*. [1988].

Photoabsorption cross sections for CH_4 compiled by *Gan* [1991] and *Gan et al*. [1992] for photons with wavelengths between 4 and 1305.45 Å are used. These include cross sections measured by *Watanabe et al*. [1953], *Ditchburn* [1955], *Rustgi* [1964], *Samson et al*. [1989], and *Lukirskii et al*. [1964]. Photoionization cross sections were obtained by *Gan et al*. [1992] from the data of *Samson et al*. [1989] and *Backx and Van der Wiel* [1975].

Liang et al. [2007] derived higher-resolution (0.04 Å) cross sections for the photoabsorption of molecular nitrogen for wavelengths between 800 and 1000 Å using a coupled-Schrodinger equation. Photons in this wavelength range have energies below the ionization threshold of N_2 (800 Å or 15.53 eV) but are capable of ionizing CH_4. *Lavvas et al*. [2011] showed that using the N_2 photoabsorption cross sections of Liang et al. significantly affects the production of CH_4^+ in the lower ionosphere. These higher-resolution cross sections are implemented only in an approximate way in the current paper by scaling the percentage of N_2 that interacts with photons using the *Gallagher et al*. [1988] cross sections in this regime and over the range of wavelengths for which this matters. Using this approach, global modelers can implement the effects of higher-resolution cross sections in a manner that is much less computationally expensive. Some of the implications are discussed in section 4.2.

2.3. Two-Stream Equations for Suprathermal Electron Flux and Electron Heating Rates

Electron impact ionization due to collisions between atmospheric neutrals and photospheric and magnetospheric electrons also contributes to ion production. Electron fluxes as a function of energy are calculated by solving the two-stream equation [*Nagy and Banks*, 1970; *Schunk and Nagy*, 2009; *Gan et al*., 1992] along magnetic field lines in 35 km intervals. Primary photoelectron production rates from the photoionization code are used as inputs. Magnetospheric inputs are not included in paper I but are considered in paper II. The field lines were assumed to have a parabolic configuration. In particular, a series of nested parabolic magnetic field lines [cf. *Richard et al*., 2011] was used to simulate the draping of Saturn's magnetic field around Titan. Radial field lines were also tried but below about 1400 km photoelectron transport is not important in any case, and the local photoelectron approximation is good [*Richard et al*., 2011; *Galand et al*., 2006, 2010; *Lavvas et al*., 2011; *Vigren et al*., 2013].

Figure 4 shows the modeled photoelectron spectrum at 1020 km for the outbound leg of the T40 flyby. The model fluxes near 10–20 eV are within about 10% of the fluxes measured by the CAPS-ELS (Cassini Plasma Spectrometer-Electron Spectrometer) instrument (shown by *Lavvas et al*. [2011] and reproduced in Figure 4). It should be noted that the CAPS electron spectra shown assumed a spacecraft potential of −0.5 eV; however, as Lavvas et al. mentioned, a spacecraft potential of −1.2 eV would bring their (and our) model calculations and CAPS-ELS data into better agreement, including the energy of the flux peak near 25 eV associated with the strong solar HeII resonance line at 30.4 nm [*Nagy and Banks*, 1970; *Gan et al*., 1992; *Robertson et al*., 2009].

As the focus of this paper is on ion production and not specifically electron impact ionization, the electron impact ionization cross sections for molecular nitrogen and methane will not be discussed here (see paper II).

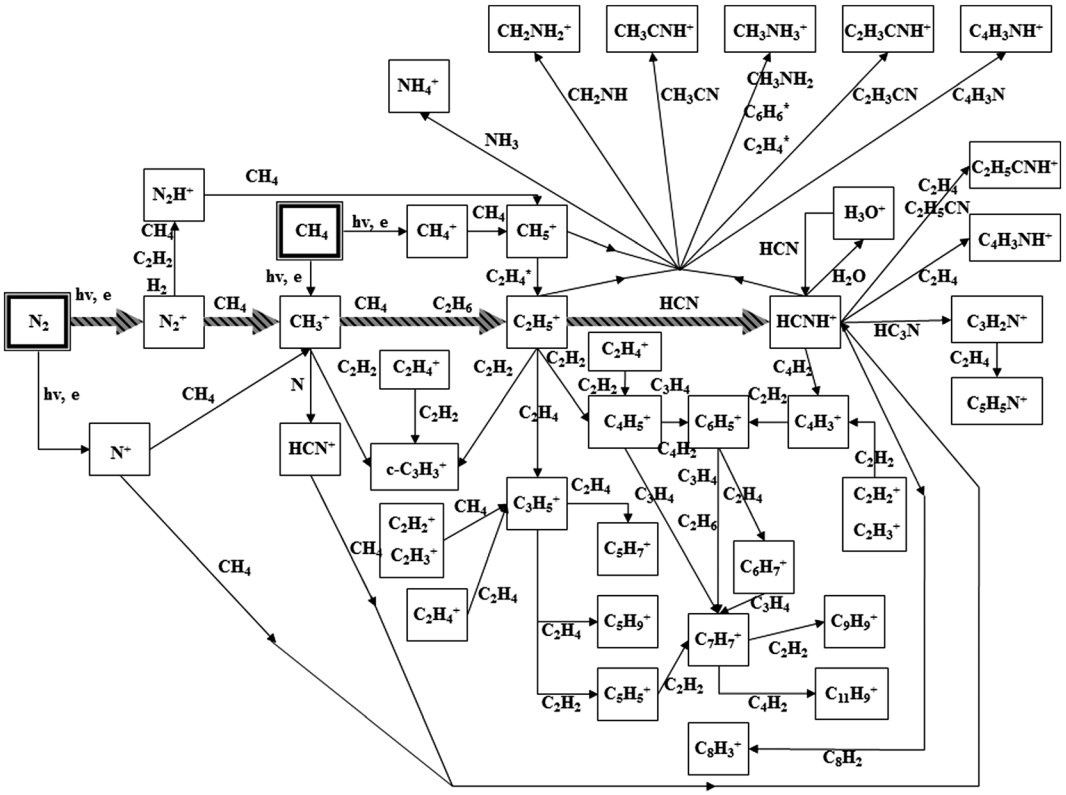

Figure 5. Ion-neutral chemical reaction scheme. Thick borders indicate the major neutral species N_2 and CH_4. Arrows show the progression of ion species through reactions with the species indicated next to the arrows. Adapted from *Cravens et al*. [2009b].

2.4. Photochemical Modeling

The photochemical model is adapted from the earlier models of *Keller et al*. [1992, 1998], *Cravens et al*. [2004], and *Robertson et al*. [2009]. This model is local, time independent, and does not include ion transport. Ion production is governed by photoionization, electron impact ionization, and chemical reactions, while the losses are dictated by chemical reactions and electron dissociative recombination. Production and loss processes are assumed to be in equilibrium, which should be a good assumption below about 1400 km [*Ma et al*., 2006, 2009; *Cravens et al*., 2010]. Solutions of the coupled photochemical equations are obtained using Newton–Raphson iterative techniques [*Press et al*., 1986]. The electron temperature profile (needed for dissociative recombination) is taken from *Richard et al*. [2011].

3. Ion Chemistry

Titan boasts a complex nitrile and hydrocarbon chemistry starting with the ionization products of the major neutral constituents of the atmosphere (N_2, CH_4, and H_2) and a host of minor neutrals which then react with neutrals to produce hydrocarbon and nitrile ion species, including those with masses well above 100 amu [*Crary et al*., 2009; *Cravens et al*., 2009b; *Vuitton et al*., 2006, 2007; *Westlake et al*., 2012]. An abridged schematic of the ion chemistry is shown in Figure 5. The progression of ion molecular growth from initial ionization to high mass terminal ions, removed primarily through electron dissociative recombination, is evident. Negative ions, which make a substantial contribution to the overall negative charge [*Ågren et al*., 2012; *Shebanits et al*., 2013], are not considered in this model.

The chemical reactions used in the model are those discussed in previous modeling exercises for Titan [*Keller et al*., 1992, 1998; *Vuitton et al*., 2007; *Cravens et al*., 2005; *Robertson et al*., 2009; *Westlake et al*., 2012]. For lower mass hydrocarbon ion species, the reaction rate coefficients compiled by *Anicich and McEwan* [1997] were used with the addition of heavier hydrocarbon reactions shown by *McEwan and Anicich* [2007]. Additional chemical

Table 2. Selected Chemical Reactions

Chemical Reaction	Reaction Rate Coefficient ($cm^3\ s^{-1}$)	% of Ion Loss at 1205 km
$N_2^+ + CH_4 \rightarrow CH_3^+$	1.04×10^{-9}	62.3%
$N_2^+ + H_2 \rightarrow HN_2^+$	2.00×10^{-9}	15.2%
$N_2^+ + CH_4 \rightarrow HN_2^+$	1.71×10^{-10}	10.3%
$N_2^+ + CH_4 \rightarrow CH_2^+$	1.03×10^{-10}	6.2%
$N_2^+ + C_2H_4 \rightarrow HCNH^+$	1.30×10^{-10}	0.4%
$N^+ + CH_4 \rightarrow CH_3^+$	5.75×10^{-10}	28.3%
$N^+ + CH_4 \rightarrow HCNH^+$	4.14×10^{-10}	20.4%
$N^+ + CH_4 \rightarrow HCN^+$	4.14×10^{-10}	20.4%
$CH_4^+ + CH_4 \rightarrow CH_5^+$	1.14×10^{-9}	73.6%
$CH_4^+ + HCN \rightarrow HCNH^+$	3.23×10^{-9}	21.3%
$CH_4^+ + C_2H_4 \rightarrow C_2H_4^+$	1.38×10^{-9}	1.01%
$CH_4^+ + C_2H_2 \rightarrow C_2H_2^+$	1.44×10^{-9}	0.98%
$CH_3^+ + CH_4 \rightarrow C_2H_5^+$	1.10×10^{-9}	91.0%
$CH_3^+ + NH \rightarrow HCNH^+$	7.40×10^{-10}	2.6%

reaction pathways for heavier hydrocarbons from reactions with benzene and nitrile species were added by *Vuitton et al.* [2006, 2007, 2008]. Recently, *Westlake et al.* [2012] highlighted the reaction rates of *Edwards et al.* [2008] for CH_2NH, C_2H_5CN, and C_2H_6 and the rates of *Zabka et al.* [2009] for reactions between $C_2H_5^+$ and benzene, which have also been implemented in our model. Based on correlations detected between different mass species, Westlake et al. also postulated several reaction pathways in which ions react with C_2 hydrocarbons (i.e., C_2H_2, C_2H_4, and C_2H_6), resulting in higher mass ions. For a reaction between ion species, *i*, and neutral species, *n*, producing ion species, *s*, the rate coefficient (units of $cm^{-3}\ s^{-1}$) is denoted k_{in}. Equation (1) shows the resulting loss rate of species i (or production rate of s), where n_n and n_i are the densities of species *n* and *i*:

$$\text{Loss}_i = \text{Prod}_s = k_{i,n} n_n, n_i \quad (1)$$

Some of the important reactions and rate coefficients are listed in Table 2.

3.1. Reaction Pathways for the Ionization Products of N_2 and CH_4

Although there are other ions that are produced through ionization of the neutral atmosphere, the ionization products of N_2 and CH_4 are the primary building blocks of the ionosphere. The ionization products of molecular nitrogen are N_2^+ and N^+. Most of the N_2^+ production, via a couple of key reactions (Figure 5 or Table 2), results in $HCNH^+$ production. This is the most abundant ion species in the ionosphere. The overwhelming majority (>99%) of N_2^+ is produced on the dayside from the photoionization and electron impact ionization of N_2. The reaction between N_2^+ and CH_4 produces CH_3^+ and accounts for upward of 65% of the loss of N_2^+ due to the large abundance of methane. For our empirical production rates, we will use CH_3^+ production as a proxy for primary N_2^+ production (with a branching factor to account for alternative loss pathways of N_2^+). Less important are reactions between methane or H_2 and N_2^+ resulting in HN_2^+, which can also produce $HCNH^+$, and a reaction with methane that produces CH_2^+. A number of reactions of $C_2H_5^+$ and $HCNH^+$ with C_2H_2, C_2H_4, and other species produce heavier hydrocarbon and nitrile ion species.

CH_4^+ is primarily produced via photoionization and electron impact ionization of methane, but reactions between H and the large amount of CH_5^+ at altitudes below 1150 km in the ionosphere contribute a nonnegligible amount (≈33%). The major chemical loss pathway for CH_4^+, accounting for more than 80% of the loss near the ionospheric peak, is through reactions with methane producing CH_5^+. The second largest sink, roughly 10–15% of the total, is through reactions with HCN to produce $HCNH^+$. The other primary ionization product of methane that impacts the ion chemistry substantially is CH_3^+. As just discussed, this species reacts with methane to produce $C_2H_5^+$ and this is the main loss process, although reaction with NH can produce $HCNH^+$.

3.2. Reaction Pathways for Intermediate and Higher Mass Ions

CH_5^+, $C_2H_5^+$, and $HCNH^+$ are typically the most abundant ions in the ionosphere, but theoretical models have had difficulties accurately reproducing density measurements [i.e., *Robertson et al.*, 2009; *Westlake et al.*, 2012]. Part of the problem is that all of these ions are chemically linked to one another, such that adjusting

Table 3. Comparison Between the Empirical and Modeled Production Rates of N_2^+

Flyby	$F_{10.7}$ Index	SZA at C/A	SZA at 1400 km	Empirical Peak N_2^+ Production Altitude (km)	EUVAC Model N_2^+ Peak Production Rate ($cm^{-3}\,s^{-1}$)	SIP Model N_2^+ Peak Production Rate ($cm^{-3}\,s^{-1}$)	Adjusted Empirical N_2^+ Peak Production Rate ($cm^{-3}\,s^{-1}$)
T40–Out	79.7	37°	15°	1075	13.1	13.6	12.7
T40–In	79.7	37°	65°	1035	10.4	10.2	10.4
T17–Out	86.7	44°	31°	1045	12.3	12.3	12.0
T17–In	86.7	45°	65°	1075	9.50	9.76	15.1
T18–Out	70.4	90°	78°	1065	2.71	3.85	4.48

the reaction pathways of one species directly impacts the other species. CH_5^+ is mainly produced from reactions between HN_2^+ and CH_4^+ and methane (Table 2), with the former reaction providing the bulk of the ion production rate. The main loss processes for CH_5^+ are reactions with HCN to produce $HCNH^+$, reactions with C_2H_2 to produce $C_2H_3^+$ and with C_2H_4 to produce $C_2H_5^+$. An overabundance of CH_5^+ will increase the production rate of $HCNH^+$ and $C_2H_5^+$. The majority of $C_2H_5^+$ is produced from reaction of CH_3^+ with methane, and the main loss process is via reactions with HCN to produce $HCNH^+$.

Approximately 80% of $HCNH^+$ production is from the reaction of HCN and $C_2H_5^+$ and 10% comes from reactions between CH_5^+ and HCN. This illustrates the importance of correctly determining the amount of HCN in the neutral atmosphere as small changes in this mixing ratio can have profound impacts on the ion chemistry of these three species. *Westlake et al.* [2012] proposed using reactions with C_2H_2 and C_2H_4 to construct higher mass ion species as motivated by the correlations they found between densities of ions whose masses differed on the order of 24 amu, the size of two carbon atoms. The impacts of these pathways on the overall electron density will be discussed in section 5 but are not the main focus of this paper.

3.3. Electron Dissociative Recombination Rates

Electron dissociative recombination coefficients and temperature dependence factors are predominantly taken from the work of *Anicich and McEwan* [1997], *McEwan and Anicich* [2007], and *Vuitton et al.* [2007]. Updated recombination coefficients from *McLain et al.* [2004], *McLain and Adams* [2009], and *Osborne et al.* [2011] for several larger ion species and for nitrile species by *Vigren et al.* [2009] and *Westlake et al.* [2012] have been implemented in the current model. For high mass molecules containing more than six carbon atoms, a reaction rate coefficient α of 1.00×10^{-6} and a temperature dependence factor $(300\,K/T_e)^{0.3}$ are assumed in this model when there are no relevant measurements.

4. Dayside Primary Ion Production Rates

Comparisons between model outputs and measurements collected during the inbound and outbound legs of the T17 and T40 flybys and the outbound leg of T18 covering a wide range of solar zenith angles (Tables 3 and 4) have been made. Theoretical ion production rates of ions will be compared with production rates derived empirically from INMS data. The outbound leg of T40 will be used to illustrate the model verification process.

Table 4. Comparison Between the Empirical and Modeled Primary Production Rates of CH_4^+

Flyby	Empirical Peak CH_4^+ Production Altitude (km)	EUVAC Model CH_4^+ Peak Production Rate ($cm^{-3}\,s^{-1}$)	SIP Model CH_4^+ Peak Production Rate ($cm^{-3}\,s^{-1}$)	Empirical CH_4^+ Peak Production Rate ($cm^{-3}\,s^{-1}$)	Percentage of Solar Photons With Wavelengths Between 800 and 1000 Å Interact With N_2 Yielding Best Agreement
T40–Out	1065	0.246	0.344	0.311	50%
T40–In	1065	0.212	0.292	0.296	50%
T17–Out	1045	0.445	0.595	0.643	50%
T17–In	1065	0.473	0.688	0.816	0%
T18–Out	1045	0.144	0.348	0.319	0%

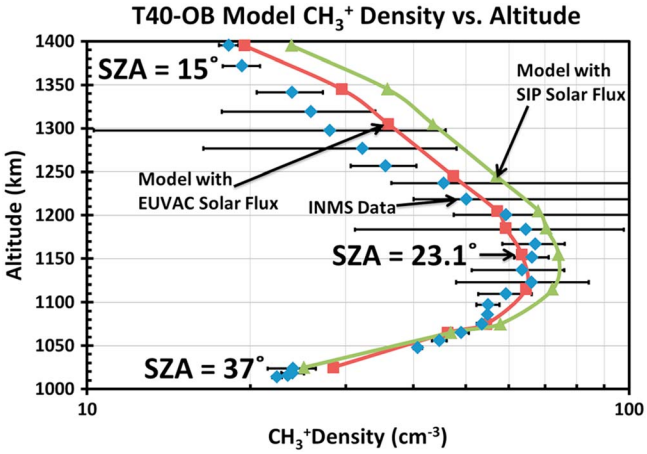

Figure 6. CH_3^+ density from the full photochemical model compared with INMS data for the T40 outbound flyby (blue diamonds). Results are shown for both the Solar Irradiance Platform (SIP), formerly SOLAR2000, and the EUVAC solar flux models (green triangles and red squares, respectively). The solar zenith angles at closest approach and at the uppermost altitude are indicated at the bottom and top of the figure. The solar zenith angle in the model calculations is adjusted to reflect the conditions along each point of the Cassini spacecraft trajectory.

4.1. N_2^+ Production Rate

The largest production rate is that of N_2^+. Unfortunately, N_2^+ has the same mass number as the most abundant ion ($HCNH^+$) which outnumbers N_2^+ by 2 to 3 orders of magnitude in all models. Hence, measured N_2^+ densities cannot be used to provide information on the production rate. Instead, we will use the density of CH_3^+ measured by INMS, since most CH_3^+ results from the reaction of N_2^+ with methane. The chemical reaction rates of *Anicich* [2003], in conjunction with the photochemical model (see section 2.4), show that 90–99% of the CH_3^+ is produced by reaction of N_2^+ with CH_4, which is then balanced by its losses via reactions with methane (the main loss process), ethylene, and NH. Figure 6 shows the CH_3^+ density profiles from the theoretical chemical model compared with INMS densities for both solar flux models. The model-data comparison is good, particularly when the EUVAC solar flux is used.

Next we consider a simplified version of the CH_3^+ chemistry and use it to obtain "empirical" N_2^+ production rates. An approximate expression for the CH_3^+ density is

$$[CH_3^+] \approx \frac{k_{N_2^+,CH_4}[N_2^+]_{model}[CH_4]}{k_{CH_3^+,CH_4}[CH_4] + k_{CH_3^+,C_2H_4}[C_2H_4] + k_{CH_3^+,NH}[NH]} \quad (2)$$

The numerator is almost equal to the primary N_2^+ production rate. An even simpler expression can be found by just keeping the first (and dominant) term in the denominator representing the main loss branch of CH_3^+. Hence, an approximate expression for the N_2^+ production rate is

$$\text{Prod } N_2^+ \approx \text{Prod } CH_3^+ \approx k_{CH3+,CH4}[CH_3^+][CH_4] \quad (3)$$

where $k_{CH3+,CH4} = 1.10 \times 10^{-9}\,cm^3\,s^{-1}$ [*Anicich*, 2003]. An "empirical" production rate is obtained by using densities measured by INMS in equation (3) (that is, $[CH_3^+]_{INMS}$ and $[CH_4]_{INMS}$).

Although the overwhelming majority of CH_3^+ is produced from N_2^+, not all N_2^+ reacts with methane to form CH_3^+. The full chemical model was used to derive a branching factor, by determining the ratio of the N_2^+ and CH_3^+ production rates. The branching factor is used to quantify the amount of N_2^+ produced that does not react to produce CH_3^+ based on our photochemical model. This ratio is shown in Figure 7 for several passes and altitudes. Sixty to eighty-five percent of the N_2^+ produced reacts with methane to form CH_3^+, but most of the values lie between 0.64 and 0.76. The production rate given by equation (3) divided by the branching factor 0.7 provides a better empirical production rate, improving the average agreement from within 39% to within 11%, and is shown alongside the theoretical production rates in Figure 8. Note that the model-measured electron density discrepancy (Figure 1) implies factors of 2–4 discrepancy in ion production and/or loss, and this branching factor, which we think we understand in any case, is a minor effect.

We have applied the above methods to several Titan flybys, and we show in some detail results from the T40 inbound and outbound, T17 inbound and outbound, and T18 outbound Cassini flybys (summarized in Table 3). Primary empirical production rates were determined with INMS densities appropriate for the individual flybys and with branching ratios for N_2^+ shown in Figure 7 and are compared to theoretical

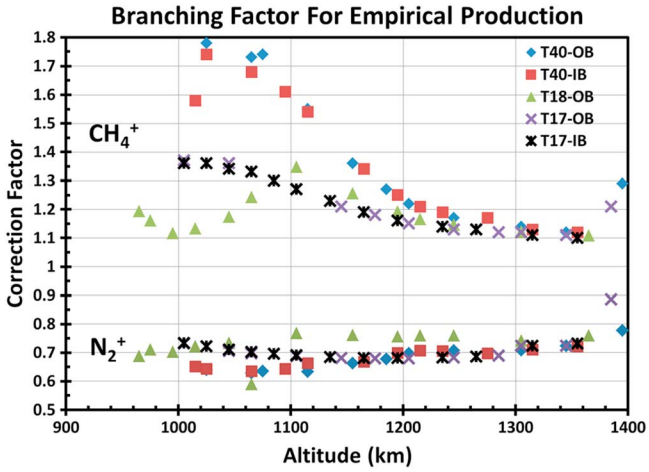

Figure 7. Branching factors for the empirical N_2^+ (below) and CH_4^+ (above) production rate found by taking the ratio of the production rates of CH_3^+ to N_2^+ in the full photochemical model. Data are shown for the inbound (red squares) and outbound (blue diamonds) legs of T40, inbound (black asterisks) and outbound (purple x's) legs of T17, and the outbound leg of T18 (green triangles).

production rates for both solar flux models. Overall, the agreement between the peak theoretical and empirical ion production rates is good, except perhaps for N_2^+ for T17 inbound. For that pass, the peak empirical ion production rate is ≈50% larger than the theoretical value, suggesting that some magnetospheric sources might be contributing in addition to solar production. This section has shown that we can use INMS-measured CH_3^+ and CH_4 densities to determine N_2^+ production rate profiles.

4.2. CH_4^+ Production Rates

We have also determined empirical CH_4^+ production rates using INMS data. Figure 9 shows CH_4^+ density profiles from the theoretical model and INMS densities for T40 outbound. In our theoretical model we are looking for a method to use low-resolution photoabsorption cross sections for N_2 to approximately account for the higher-resolution theoretical N_2 photoabsorption cross sections for photons between 800 and 1000 Å published by *Liang et al.* [2007] and utilized by *Lavvas et al.* [2011]. To do this, we assume that at wavelengths where the high-resolution cross section is very large, all the photons are absorbed, and where the cross section is low, the photons are absorbed according to the low-resolution photoabsorption cross sections of N_2 of *Gallagher et al.* [1988]. Our model has 17 wavelength bins in the 800–1000 Å region of the spectrum. The issue is then what is the statistical wavelength coverage of the low/high cross sections. After trying different values we settled on 50% for 800–1000 Å as this gives good agreement with the empirical CH_4^+ production rate at low altitudes as discussed below and also gives agreement with the results of *Lavvas et al.* [2011]. The EUVAC solar model gives better agreement overall than the SIP solar fluxes.

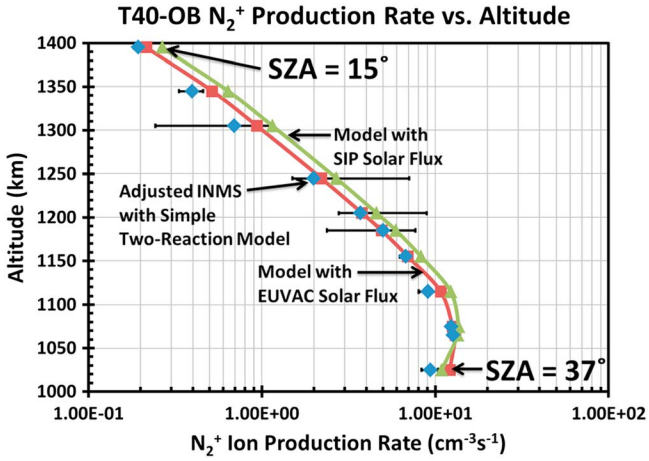

Figure 8. Model photoionization N_2^+ production rates (including photoelectron ionization) compared with empirical production rates (from INMS data, as described in the text) for the T40 outbound flyby (blue diamonds). Model results for the SIP and EUVAC solar fluxes are shown as green triangles and red squares, respectively. The solar zenith angles at closest approach and at the uppermost altitude are indicated at the bottom and top of the figure.

Next we consider a simple expression for a CH_4^+ empirical primary production rate. Primary ionization of methane by photons and photoelectrons accounts for roughly 65% of the total production of CH_4^+. Other sources include CH_5^+ reacting with H, and H_2^+, H^+, and N^+ reacting with methane. More than 90% of the loss of CH_4^+ is due to the reaction with methane (rate coefficient of $k_{CH4+,CH4} = 1.14 \times 10^{-9}\ cm^3\ s^{-1}$ [*Anicich*, 2003]). Hence, the total production rate of CH_4^+ (not just the primary production) is given by the following expression to within a few percent:

$$Prod_{CH4+} = k_{CH4+,CH4}[CH_4^+][CH_4] \quad (4)$$

An empirical production rate is provided by equation (4) if measured densities ($[CH_4^+]_{INMS}$ and $[CH_4]_{INMS}$) instead of

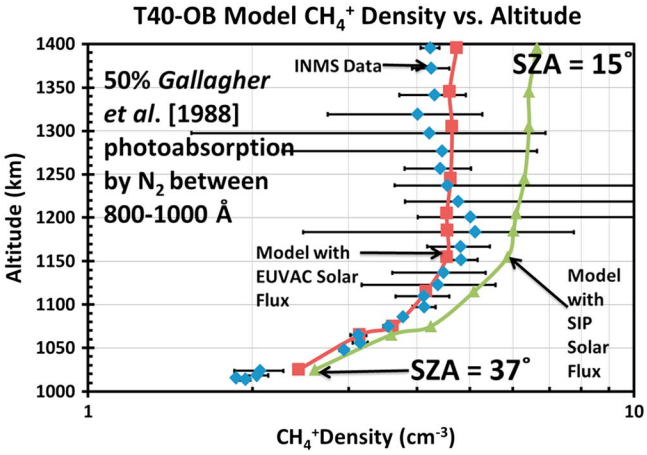

Figure 9. CH_4^+ density from the full photochemical model compared with INMS data for T40 outbound. See text for details. The solar zenith angles at closest approach and at the uppermost altitude are indicated at the bottom and top of the figure.

model densities are used in this expression. However, to obtain an empirical production rate for the primary ionization rate of methane (leading to CH_4^+), we must exclude the nonprimary chemical sources of this species, which we do by obtaining another branching factor suggested by the full theoretical model calculations. For this case, the branching factor is the ratio of total rate of CH_4^+ production (photoionization, electron impact ionization, and chemical reactions) to the rate of that produced via photoionization and electron impact ionization. Dividing equation (4) by this branching factor (Figure 7) yields an empirical primary production rate. Figure 10 shows the results for the T40 outbound flyby.

Once again, this method was applied to the inbound and outbound legs of T40, inbound and outbound legs of T17 and the outbound leg of T18 (Table 4), and the empirical (including the branching factors in Figure 7) and modeled production rates are found to be in reasonable agreement. We note that below about 1150 km altitude the empirical and theoretical CH_4^+ production rates are not entirely independent due to the comparison we used to obtain the 50% low-/high-resolution N_2 cross section factor (but we also used comparison with the CH_4^+ production from *Lavvas et al.* [2011] to find this, which is independent).

In this section we showed that the relatively "primary" ion species CH_3^+ and CH_4^+ as measured by INMS agree very well with photochemical models, and, which is really the same thing, the empirical INMS and theoretical N_2^+ and CH_4^+ ion productions agree well. This suggests that we do understand the primary ionization process on the dayside and that the problem with the theoretical models lies in the losses and not the sources. We have also demonstrated that INMS ion and neutral data can be used to generate primary ion production rates which can be useful when the means do not exist to run a complete theoretical model.

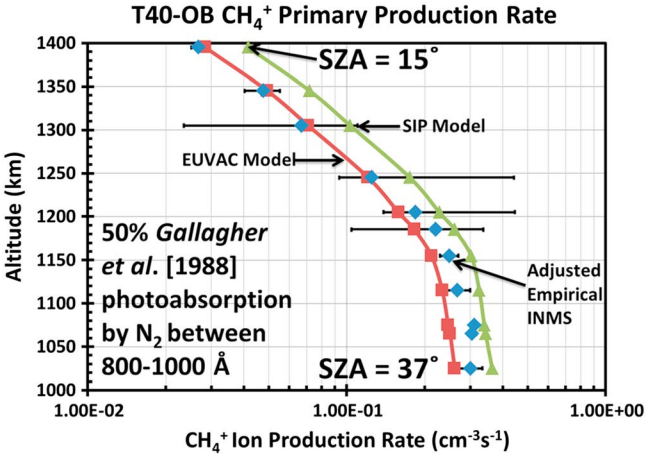

Figure 10. Modeled CH_4^+ production rates from the full photochemical model compared with empirical CH_4^+ production rates for T40 outbound (see text).

4.3. Primary Ion Production Rate Profiles Across the Dayside

Several applications require global ion production rates (e.g., global MHD and hybrid models [*Ma et al.*, 2007, 2009; *Ulusen et al.*, 2010]). In order to make these available for solar minimum conditions, we calculated primary ion production rates for a full range of solar zenith angles using the global averaged major neutral densities discussed earlier. The T40 EUVAC solar photon flux model was adopted, and we assumed half of the solar photons between 800 and 1000 Å interact with N_2 using the cross sections of *Gallagher et al.* [1988]. We used a magnetic field topology with large horizontal components so that photoelectron transport was not

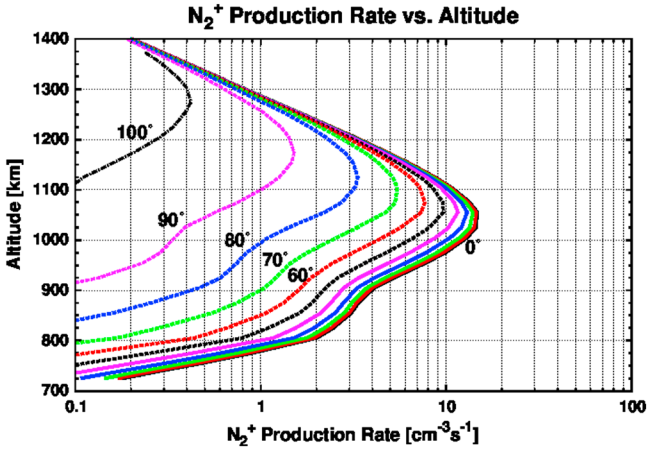

Figure 11. Production rate of N_2^+ resulting from the photoionization and photoelectron impact ionization for the global average neutral model of the ionosphere using the EUVAC model of the solar photon flux for T40 conditions ($F_{10.7} = 79.7$) and nested magnetic field lines for solar zenith angles between 0° and 100° in 10° increments.

important. Figures 11 and 12 show the total primary N_2^+ and CH_4^+ production rates from the above exercise.

Models also require N^+ production from ionization of N_2 and CH_3^+, CH_2^+, CH^+, C^+, H_2^+, and H^+ from the ionization of CH_4 in addition to N_2^+ and CH_4^+ production. We show our model production rates for the T40 flyby and a solar zenith angle of 60° in Figure 13. A comparison of these production rate profiles with profiles for the T40 flyby (and a solar zenith angle of 60°) from *Lavvas et al.* [2011] shows agreement to within 15%.

We used these global ion production rates in our chemical model and obtained an effective electron recombination rate of 1.01×10^{-6} cm^3 s^{-1} by dividing our total (all ion species) primary production rate at the peak by the RPWS/LP peak electron density at 60° squared ($\alpha_{\text{eff}} = P/n_e^2$). The effective peak model electron density versus solar zenith angle was determined by finding the total ion production rate from Figures 11–13 and using the above effective recombination rate coefficient. Figure 1 shows these effective peak electron densities. The divergence from RPWS values at lower solar zenith angles indicates that the effective recombination coefficient cannot be a constant. *Galand et al.* [2010] estimated an effective recombination rate coefficient of 5.9×10^{-6} cm^3 s^{-1} at 970 km. *Kliore et al.* [2011] and *Vigren et al.* [2013] estimated values at 1100 km of 1×10^{-6} cm^3 s^{-1} and 3×10^{-6}cm^3 s^{-1}, respectively, which are about an order of magnitude larger than most "standard" photochemical models with RPWS/LP electron temperatures (2.5×10^{-7} cm^3 s^{-1}) [*Cravens et al.*, 2005; *Krasnopolsky*, 2009]. Our estimates using the empirical production rates for T40 outbound conditions and RPWS electron densities are 2.07×10^{-6} cm^3 s^{-1} at 1025 km and 1.55×10^{-6} cm^3 s^{-1} at 1115 km.

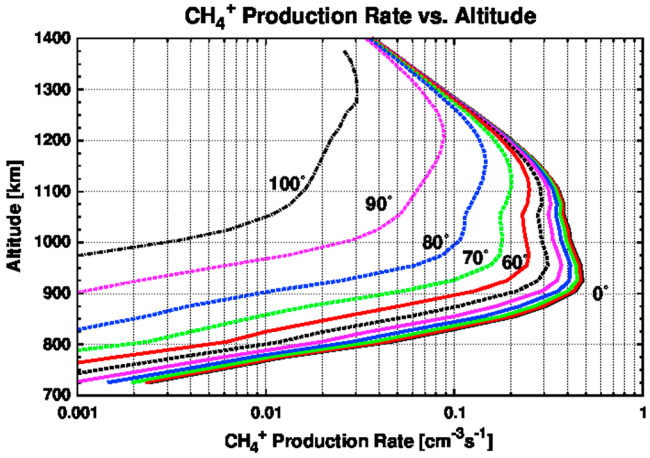

Figure 12. Production rate of CH_4^+ resulting from the photoionization and photoelectron impact ionization of the global average model of the ionosphere of Titan using the EUVAC model of the solar photon flux for T40 conditions ($F_{10.7} = 79.7$) and nested magnetic field lines for solar zenith angles between 0° and 100° in 10° increments. In this model half of the solar photons between 800 and 1000 Å interact with molecular nitrogen using the cross sections of *Gallagher et al.* [1988] to approximately simulate the higher-resolution cross sections of *Liang et al.* [2007].

4.4. Empirical Production Rates Across the Dayside

By applying the simple two-reaction model (and a branching factor of 0.67) to INMS ion and neutral density measurements, empirical N_2^+ production rates were determined for all suitable dayside Cassini flybys up to T86 (Figure 14). The peak production rate decreases as the solar zenith angle increases as expected.

Figure 14 shows a general agreement with Figure 11 in peak production at a given solar zenith angle (SZA) and an increasing altitude of peak production with SZA as qualitatively expected for a Chapman layer. But there is also a lot of variation, particularly above 1200 km where the different curves should converge as shown in Figure 11. This is

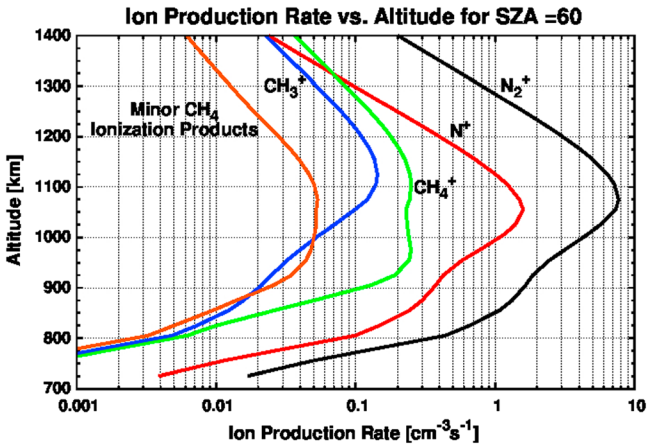

Figure 13. Production rates for primary ionization (photons and photoelectron contributions) products of N_2 and CH_4 for a solar zenith angle of 60° for T40 conditions ($F_{10.7} = 79.7$). The orange curve shows the combined production rates of CH_2^+, CH^+, C^+, H_2^+, and H^+.

due to neutral density differences for different flybys as a single global neutral atmosphere model for all locations is not entirely accurate. At lower altitudes, magnetospheric sources could be contributing, which is a possible explanation for the increase in the production rates for the T32 and T59 outbound flybys below 1100 km.

Figure 15 shows the peak ion production rate of N_2^+ plotted against altitude and solar zenith angle. Examining the peak empirical production rates for flybys between T17 and T86 indicates that our method is producing reasonable results. Between solar zenith angles of 0° and 60°, the empirical peak production rate is between 10 and 11 $cm^{-3}\,s^{-1}$. This range of production rates corresponds to an electron density between 3150 cm^{-3} and 3300 cm^{-3}, when using a recombination rate of 1.01 $cm^3\,s^{-1}$ as described above. This value is within 10% of the electron densities reported by RPWS/LP [*Ågren et al.*, 2009] (Figure 1). Similarly, the empirical production rate decreases as the solar zenith angle increases. These rates vary by more than 50% near 1000 km and 25% around 1200 km. These variations are to be expected as the neutral atmosphere and solar conditions vary between collected flybys.

5. Discussion of Ion Loss Processes

Although our photochemical model solves for 136 ion species, the current paper has focused on primary ion species. The previous sections indicate that modeled primary ion production rates are reasonable. Hence, the excessively high electron densities produced by models must be due to problems with the chemistry (ion-ion neutralization, dissociative ionization, ion molecule reactions, negative ion chemistry) and dissociative recombination rate coefficients. In this section, we used the model to explore how the theoretical electron and ion densities can be brought into better agreement with RPWS/LP electron densities (Figure 1) and INMS ion densities [*Mandt et al.*, 2012].

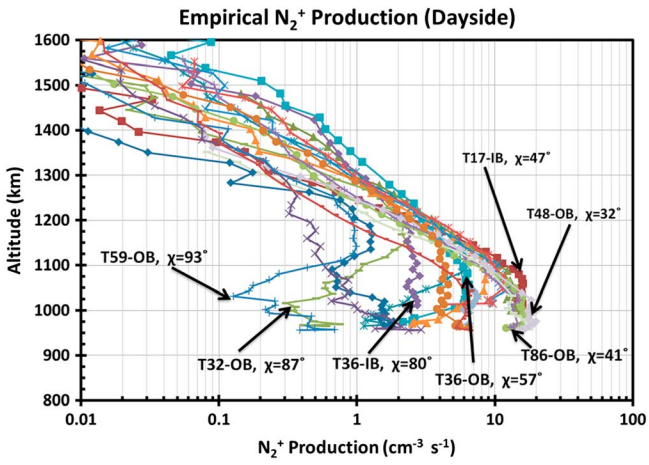

Figure 14. Empirical N_2^+ production rates derived using INMS measurements and the simple two-reaction model and including the correction factor of 0.67 discussed in the text. Flybys number and solar zenith angle at closest approach are indicated for selected passes.

The effective electron dissociative recombination rate can be increased either by lowering the thermal electron temperature [e.g., *Richard et al.*, 2011] or by reacting lower mass ions to produce higher mass ions that have higher dissociative recombination coefficients. Richard et al. demonstrated that electron temperatures are strongly coupled to the neutral temperature of 150 K below 1000 km, due to the large thermal coupling with neutrals. At the ionospheric peak the modeled and RPWS-measured electron temperatures differ by less than 10% for the T40 flyby. This indicates that using modeled electron temperatures will not significantly alter the modeled peak ion densities. As the modeled

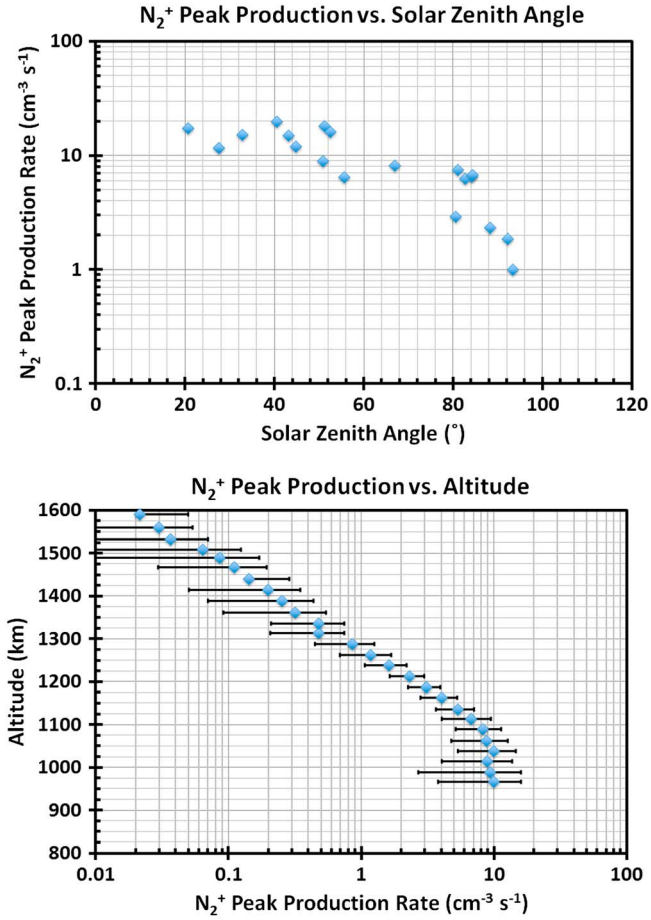

Figure 15. Empirical peak production rate of N_2^+ computed using the methodology described in section 4 and extracted from Figure 14 plotted against solar zenith angle (above) and altitude (below).

temperatures did not decrease the electron density sufficiently at higher altitudes, ion-neutral chemistry will be examined.

Modeling the chemical processes in the ionosphere has proven to be a challenging endeavor [cf. *Robertson et al.*, 2009; *Cui et al.*, 2009; *Galand et al.*, 2010; *Westlake et al.*, 2012; *Vigren et al.*, 2013; *Vuitton et al.*, 2006, 2007; *Wilson and Atreya*, 2004; *Krasnopolsky*, 2009]. *Westlake et al.* [2012] proposed reactions between $HCNH^+$ and C_2H_2 and $HCNH^+$ and C_2H_4 with a reaction rate coefficient of 5.00×10^{-11} cm^3 s^{-1} and a threefold increase in the density of C_2H_2 and C_2H_4 relative to the ratios of *Magee et al.* [2009]. These reactions proved helpful in moving the ions from $HCNH^+$, which had a previously modeled ion density factor of 4 larger than the value measured by the INMS instrument to within a factor of 2. Implementing these reaction pathways also improved the electron density agreement between the model and RPWS/LP by 15% to within a factor of 2.5.

Even with these modifications, the modeled electron density is still too large, as is the density of the major ion species, $HCNH^+$. In order to illustrate this point, altitude profiles of measured and modeled $HCNH^+$ densities are shown in Figure 16. Figure 16 shows that a tenfold increase to the $HCNH^+$ dissociative recombination rate coefficient brought the measured and modeled $HCNH^+$ densities into better, but not perfect, agreement. This increased recombination coefficient brings the total ion-electron recombination rate at 1205 km to 3.5×10^{-6} cm^3 s^{-1}, which is in the range of the recombination rates estimated by *Galand et al.* [2010] between 970 and 1200 km (5.9×10^{-6} and 6.9×10^{-7} cm^3 s^{-1}, respectively). This illustrates the importance of constraining the loss mechanisms for this important species as it accounts for the majority of the discrepancy between the modeled and measured ion and electron densities.

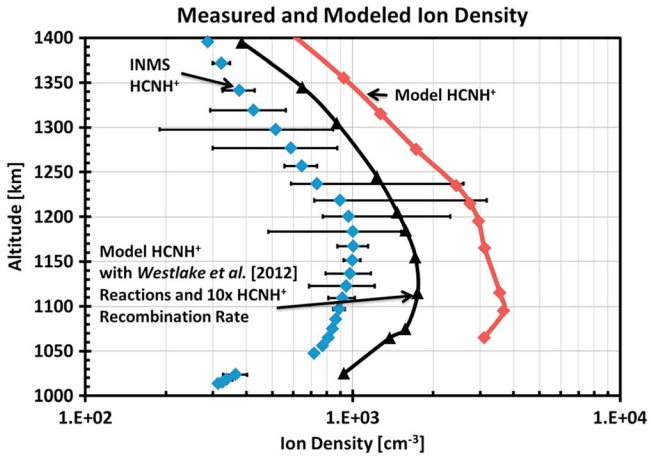

Figure 16. Comparisons between the INMS measured (blue diamonds) $HCNH^+$ density and modeled for the three model cases discussed in the text.

6. Conclusions

In summary, the following key conclusions can be made concerning the dayside ionosphere of Titan:

1. The discrepancy between modeled and measured (INMS, RSS, and RPWS/LP) electron and ion densities is not due to overproduction of the primary ion species and therefore must be caused by insufficient electron-ion recombination, other chemistries (i.e., ion molecule reactions), or the contributions of negative ions to the total charge [*Ågren et al*., 2012; *Shebanits et al*., 2013; *Vuitton et al*., 2009].
2. Solar flux empirical models (i.e., EUVAC and SOLAR2000) only make a 25% difference in the modeled ion production rates.
3. Allowing 50% of solar photons with wavelengths between 800 and 1000 Å to interact with molecular nitrogen using the low-resolution photoabsorption cross sections of *Gallagher et al*. [1988] provides a reasonable approximation to the high-resolution photoabsorption cross sections of *Liang et al*. [2007] for CH_4^+ production, confirming the analysis of *Lavvas et al*. [2011].
4. Using the chemical reaction pathways of *Anicich and McEwan* [1997], *McEwan and Anicich* [2007], and *Vuitton et al*. [2006, 2007] with updated reaction rate coefficients observed by *Edwards et al*. [2008] and *Zabka et al*. [2009] requires that the electron dissociative recombination rate coefficient for $HCNH^+$ be increased by at least a factor of 10 (if this is really the explanation for the high electron densities). The required increased loss rate could be due to processes leading from $HCNH^+$ and $C_2H_5^+$ to higher mass ion species, followed by increased recombination. In order to effectively resolve both of these conflicts research must be conducted into reaction pathways for $HCNH^+$ and the dissociative electron recombination of this ion.
5. Production rate profiles for the major primary ionization products of N_2 and CH_4 have been generated for solar zenith angles between 0° and 100°. This will enable future modelers of the ionosphere of Titan to construct generic primary ion production rate profiles representing conditions of interest to them.
6. Empirical production rate profiles of N_2^+ and CH_4^+ have been constructed using simple two-reaction chemistry and densities measured by INMS. This procedure provides ion production rates for situations in which theoretical values are not available, but INMS data are available.

Acknowledgments

The research described in this paper was supported at the University of Kansas by NASA Cassini grant NA57-03001 via subcontract from the Southwest Research Institute and by NASA Planetary Atmospheres grant NNX10AB86G. Solar Irradiance Platform historical irradiances are provided courtesy of W. Kent Tobiska and Space Environment Technologies. These historical irradiances have been developed with partial funding from the NASA UARS, TIMED, and SOHO missions. All Cassini data, including INMS data, are or soon will be available through the Planetary Data System.

Michael Liemohn thanks the reviewers for their assistance in evaluating this paper.

References

Acton, L., D. C. Weston, and M. E. Bruner (1999), Deriving solar X ray irradiance from Yohkoh observations, *J. Geophys. Res.*, *104*, 14,827–14,832, doi:10.1029/1999JA900006.

Agren, K., et al. (2007), On magnetospheric electron impact ionization and dynamics in Titan's ram-side and polar ionosphere—A Cassini case study, *Ann. Geophys.*, *25*, 2359–2369.

Ågren, K., J.-E. Wahlund, P. Garnier, R. Modolo, J. Cui, M. Galand, and I. Muller-Wodarg (2009), On the ionospheric structure of Titan, *Planet. Space Sci.*, *57*(14–15), 1821–1827, doi:10.1016/j.pss.2009.04.012.

Ågren, K., N. J. T. Edberg, and J.-E. Wahlund (2012), Detection of negative ions in the deep ionosphere of Titan during the Cassini T70 flyby, *Geophys. Res. Lett.*, *39*, L10201, doi:10.1029/2012GL051714.

Anicich, V. (2003), *An Index of the Literature for Bimolecular Gas Phase Cation-Molecule Reaction Kinetics*, vol. 03–19, pp. 1–28, 53–262, 668–701, NASA, Jet Propul. Lab., Calif. Inst. of Technol., Pasadena, Calif.

Anicich, V., and M. McEwan (1997), Ion-molecule chemistry in Titan's ionosphere, *Planet. Space Sci.*, *45*(8), 897–921.

Backx, C., and M. J. Van der Wiel (1975), Electron-ion coincidence measurements of CH_4, *J. Phys. B.*, *8*, 3020.

Banaskiewicz, M., L. M. Lara, R. Rodrigo, J. J. Lopez-Moreno, and G. J. Molina-Cuberos (2000), A coupled model of Titan's atmosphere and ionosphere, *Icarus*, *147*, 386–404.

Banks, P. M., and G. Kockarts (1973), *Aeronomy, Parts A and B*, Academic Press, Inc., New York.

Bird, M. K., R. Dutta-Roy, S. W. Asmar, and T. A. Rebold (1997), Detection of Titan's ionosphere from Voyager 1 radio occultation observations, *Icarus*, *130*, 426–436.

Coates, A. J., F. J. Crary, G. R. Lewis, D. T. Young, and E. C. Sittler Jr. (2007), Discovery of heavy negative ions in Titan's ionosphere, *Geophys. Res. Lett.*, *34*, L22103, doi:10.1029/2007GL030978.

Crary, F. J., B. A. Magee, K. Mandt, J. H. Waite Jr., J. Westlake, and D. T. Young (2009), Heavy ion temperatures and winds in Titan's ionosphere: Combined Cassini CAPS and INMS observations, *Planet. Space Sci.*, *57*(14–15), 1847–1856.

Cravens, T., et al. (2006), Composition of Titan's ionosphere, *Geophys. Res. Lett.*, *33*, L07105, doi:10.1029/2005GL025575.

Cravens, T. E., J. Vann, J. Clark, J. Yu, C. N. Keller, and C. Brull (2004), The ionosphere of Titan: An updated theoretical model, *Adv. Space Res.*, *33*, 212–215.

Cravens, T. E., et al. (2005), Titan's ionosphere: Model comparisons with Cassini Ta data, *Geophys. Res. Lett.*, *32*, L12108, doi:10.1029/2005GL023249.

Cravens, T. E., I. P. Robertson, S. A. Ledvina, D. Mitchell, S. M. Krimigis, and J. H. Waite Jr. (2008), Energetic ion precipitation at Titan, *Geophys. Res. Lett.*, *35*, L03103, doi:10.1029/2007GL032451.

Cravens, T. E., et al. (2009a), Model–data comparisons for Titan's nightside ionosphere, *Icarus*, *199*, 174.

Cravens, T. E., R. V. Yelle, J.-E. Wahlund, D. E. Shemansky, and A. F. Nagy (2009b), Composition and structure of the ionosphere and thermosphere, in *Titan From Cassini-Huygens*, edited by R. H. Brown, J.-P. Lebreton, and J. H. Waite Jr., pp. 259–296, Springer, New York.

Cravens, T. E., et al. (2010), Dynamical and magnetic field time constants for Titan's ionosphere: Empirical estimates and comparisons with Venus, *J. Geophys. Res.*, *115*, A08319, doi:10.1029/2009JA015050.

Cui, J., et al. (2009), Analysis of Titan's neutral upper atmosphere from Cassini Ion Neutral Mass Spectrometer measurements, *Icarus*, *200*, 581.

De la Haye, V., J. H. Waite Jr., T. E. Cravens, I. P. Robertson, and S. Lebonnois (2008), Coupled ion and neutral rotating model of Titan's upper atmosphere, *Icarus*, *197*(1), 110–136, doi:10.1016/j.icarus.2008.03.022.

Denne, D. R. (1970), Measurements of the ultrasoft X-ray absorption of Ar, Ne, N_2, O_2, CH_4, He and H_2, *J. Phys. D.*, *3*, 1392.

Ditchburn, R. W. (1955), Absorption cross-sections in the vacuum ultra-violet. III, Methane, *Proc. R. Soc. London*, *229A*, 44.
Edberg, N. J. T., J.-E. Wahlund, K. Ågren, M. W. Morooka, R. Modolo, C. Bertucci, and M. K. Dougherty (2010), Electron density and temperature measurements in the cold plasma environment of Titan: Implications for atmospheric escape, *Geophys. Res. Lett.*, *37*, L20105, doi:10.1029/2010GL044544.
Edberg, N. J. T., D. J. Andrews, O. Shebanits, K. Ågren, J.–E. Wahlund, H. J. Opgenoorth, T. E. Cravens, and Z. Girazian (2013a), Solar cycle modulation of Titan's ionosphere, *J. Geophys. Res. Space Physics*, *118*, 5255–5264, doi:10.1002/jgra.50463.
Edberg, N. J. T., et al. (2013b), Extreme densities in Titan's ionosphere during the T85 magnetosheath encounter, *Geophys. Res. Lett.*, *40*, 2879–2883, doi:10.1002/grl.50579.
Edwards, S., C. Freeman, and M. McEwan (2008), The ion chemistry of methylenimine and propionitrile and their relevance to Titan, *Int. J. Mass Spectrom.*, *272*(1), 86–90.
Galand, M., J. Lilensten, D. Toublanc, and S. Maurice (1999), The ionosphere of Titan: Ideal diurnal and nocturnal cases, *Icarus*, *140*, 92–105.
Galand, M., R. V. Yelle, A. J. Coates, H. Backes, and J.-E. Wahlund (2006), Electron temperature of Titan's sunlit ionosphere, *Geophys. Res. Lett.*, *33*, L21101, doi:10.1029/2006GL027488.
Galand M., R. Yelle, J. Cui, J.-E. Wahlund, V. Vuitton, A. Wellbrock, and A. Coates (2010), Ionization sources in Titan's deep ionosphere, *J. Geophys. Res.*, *115*, A07312, doi:10.1029/2009JA015100.
Gallagher, J. W., C. E. Brion, J. A. Samson, and P. W. Langhoff (1988), Absolute cross sections for molecular photoabsorption, partial photoionization, and ionic photofragmentation processes, *J. Phys. Chem. Ref. Data*, *17*, 9.
Gan, L. (1991), Electron distributions and solar wind interaction with nonmagnetic planets, PhD dissertation, Univ. of Michigan, Ann Arbor, Mich.
Gan, L., C. N. Keller, and T. E. Cravens (1992), Electrons in the ionosphere of Titan, *J. Geophys. Res.*, *97*, 12,136–12,151.
Gronoff, G., J. Lilensten, L. Desorgher, and E. Fluckiger (2009a), Ionization processes in the atmosphere of Titan I. Ionization in the whole atmosphere, *Astron. Astrophys.*, *506*, 955–964.
Gronoff, G., J. Lilensten, and R. Modolo (2009b), Ionization processes in the atmosphere of Titan II. Electron precipitation along magnetic field lines, *Astron. Astrophys.*, *506*, 965–970.
Kasprzak, W. K., et al. (1996), Cassini orbiter ion and neutral mass spectrometer, *Proc. SPIE*, *2803*, 129.
Keller, C. N., T. E. Cravens, and L. Gan (1992), A model of the ionosphere of Titan, *J. Geophys. Res.*, *97*, 12,117–12,135, doi:10.1029/92JA00231.
Keller, C. N., V. G. Anicich, and T. E. Cravens (1998), Model of Titan's ionosphere with detailed hydrocarbon chemistry, *Planet. Space Sci.*, *46*, 1157–1174.
Kliore, A. J., et al. (2008), First results from the Cassini radio occultations of the Titan ionosphere, *J. Geophys. Res.*, *113*, A09317, doi:10.1029/2007JA012965.
Kliore, A. J., A. F. Nagy, T. E. Cravens, M. S. Richard, and A. M. Rymer (2011), Unusual electron density profiles observed by Cassini radio occultations in Titan's ionosphere: Effects of enhanced magnetospheric electron precipitation?, *J. Geophys. Res.*, *116*, A11318, doi:10.1029/2011JA016694.
Krasnopolsky, V. (2009), A photochemical model of Titan's atmosphere and ionosphere, *Icarus*, *201*, 226–256.
Langhoff, P. W., S. R. Langhoff, T. N. Rescigno, J. Schirmer, L. S. Cedarbaum, W. Dorncke, and W. Won Niessen (1981), Theoretical studies of inner-valence-shell photoionization cross sections in N_2 and CO, *Chem. Phys.*, *58*, 71.
Lavvas, P. P., A. Coustenis, and I. M. Vardavas (2008a), Coupling photochemistry with haze formation in Titan's atmosphere. Part I. Model description, *Planet. Space Sci.*, *56*, 27–66.
Lavvas, P. P., A. Coustenis, and I. M. Vardavas (2008b), Coupling photochemistry with haze formation in Titan's atmosphere. Part II. Results and validation with Cassini/Huygens data, *Planet. Space Sci.*, *56*, 67–99.
Lavvas, P., M. Galand, R. V. Yelle, A. N. Heays, B. R. Lewis, G. R. Lewis, and A. J. Coates (2011), Energy deposition and primary chemical products in Titan's upper atmosphere, *Icarus*, *213*, 233–251, doi:10.1016/j.icarus.2011.03.001.
Liang, M.-C., A. N. Heays, B. R. Lewis, S. T. Gibson, and Y. L. Yung (2007), Source of nitrogen isotope anomaly in HCN in the atmosphere of Titan, *Astrophys. J.*, *664*, L115–L118.
Lilensten, J., O. Witasse, C. Simon, H. Soldi-Lose, O. Dutuit, R. Thissen, and C. Alcaraz (2005a), Prediction of a N^{++} 2 layer in the upper atmosphere of Titan, *Geophys. Res. Lett.*, *32*, L03203, doi:10.1029/2004GL021432.
Lilensten, J., C. Simon, O. Witasse, O. Dutuit, R. Thissen, and C. Alcarez (2005b), A fast comparison of the diurnal secondary ion production in the ionosphere of Titan, *Icarus*, *174*, 285–288.
Luhmann, J. G., et al. (2012), Investigating magnetospheric interaction effects of Titan's ionosphere with the Cassini orbiter Ion Neutral Mass Spectrometer, Langmuir Probe and magnetometer observations during targeted flybys, *Icarus*, *219*, 534–555, doi:10.1016/j.icarus.2012.03.015.
Lukirskii, A. P., I. A. Brytov, and T. M. Zimkina (1964), Photoionization absorption of He, Kr, Xr, CH_4 and methylal in the 23.6-250 Å region, *Opt. Sprctrosc. USSR, English Transl.*, *17*, 234.
Ma, Y., A. F. Nagy, T. E. Cravens, I. V. Sokolov, K. C. Hansen, J.-E. Wahlund, F. J. Crary, A. J. Coates, and M. K. Dougherty (2006), Comparisons between MHD model calculations and observations of Cassini flybys of Titan, *J. Geophys. Res.*, *111*, A05207, doi:10.1029/2005JA011481.
Ma, Y.-J., et al. (2007), 3D global multi-species Hall-MHD simulation of the Cassini T9 flyby, *Geophys. Res. Lett.*, *34*, L24S10, doi:10.1029/2007GL031627.
Ma, Y.-J., et al. (2009), Time-dependent global MHD simulations of Cassini T32 flyby: From magnetosphere to magnetosheath, *J. Geophys. Res. 114*, A03204, doi:10.1029/2008JA013676.
Magee, B., J. Bell, J. H. Waite Jr., K. Mandt, J. Westlake, and D. Gell (2009), INMS derived composition of Titan's upper atmosphere: Analysis methods and model comparison, *Planet. Space Sci.*, *57*, 1895–1916.
Mandt, K. E., J. H. Waite Jr., B. Teolis, B. A. Magee, J. Bell, J. Westlake, C. Nixon, O. Mousis, and J. Lunine (2012), The 12C/13C ratio on Titan from Cassini INMS measurements and implications for the evolution of methane, *Astrophys. J.*, *749*, 160, doi:10.1088/0004-637X/749/2/160.
McEwan, M. J., and V. G. Anicich (2007), Titan's ion chemistry: A laboratory perspective, *Mass Spectrom. Rev.*, *26*, 281–319.
McLain, J., and N. Adams (2009), Flowing afterglow studies of temperature dependencies for electron dissociative recombination of $HCNH^+$, CH_3CNH^+, $CH_3CH_2CNH^+$ and their symmetrical proton-bound dimers, *Planet. Space Sci.*, *57*(13), 1642–1647.
McLain, J., V. Poterya, D. Christopher, L. Babcock, and N. Adams (2004), Flowing afterglow studies of the temperature dependencies for dissociative recombination of O_2^+, CH_5^+, $C_2H_5^+$, and $C_6H_7^+$ with electrons, *J. Chem. A*, *108*(32), 6704–6708.
Molina-Cuberos, G. J., H. Lammer, W. Stumptner, K. Schwingenschuh, H. O. Rucker, J. J. Lopez-Moreno, K. Rodrigo, and T. Tokano (2001), Ionosphere layer induced by meteoric ionization in Titan's atmosphere, *Planet. Space Sci.*, *49*, 143–153.
Nagy, A. F., and P. M. Banks (1970), Photoelectron fluxes in the ionosphere, *J. Geophys. Res.*, *75*, 6260–6270, doi:10.1029/JA075i031p06260.
Osborne, D., P. Lawson, and N. Adams (2011), The effect of N-heteroatoms and CH_3 substituents on dissociative electron-ion recombination of protonated single six membered ring compounds at room temperature, *Int. J. Mass Spectrom.*, *308*(1), 4.

Press, W. H., B. P. Flannery, S. A. Teukolsky, and W. T. Vetterling (1986), Numerical recipes, in *269–273*, Cambridge Univ. Press, New York.
Richard, M. S., T. E. Cravens, I. P. Robertson, J. H. Waite, J.-E. Wahlund, F. J. Crary, and A. J. Coates (2011), Energetics of Titan's ionosphere: Model comparisons with Cassini data, *J. Geophys. Res.*, *116*, A09310, doi:10.1029/2011JA016603.
Richards, P. G., J. A. Fenelly, and D. G. Torr (1994), EUVAC: A solar flux model for aeronomic calculations, *J. Geophys. Res.*, *99*, 8981–8992, doi:10.1029/94JA00518.
Robertson, I. P., et al. (2009), Structure of Titan's ionosphere: Model comparisons with Cassini data, *Planet. Space Sci.*, *57*, 1834, doi:10.1016/j.pss.2009.07.011.
Roboz, A., and A. F. Nagy (1994), The energetics of Titan, *Geophys. Res. Lett.*, *99*, 2087–2093, doi:10.1029/93JA02286.
Rustgi, O. P. (1964), Absorption cross sections of argon and methane between 600 and 170 Å, *J. Opt. Soc. Am.*, *54*, 464.
Samson, J. A. R., G. N. Haddad, T. Masuoka, P. N. Pareek, and D. A. L. Kilcoyne (1989), Ionization yields, total absorption, and dissociative photoionization cross sections of CH_4 from 110–950 Å, *J. Chem. Phys.*, *90*(12), 6925.
Schunk, R. W., and A. F. Nagy (2009), *Ionospheres*, 2nd ed., Cambridge Univ. Press, Cambridge, U. K.
Shebanits, O., J.-E. Wahlund, K. Mandt, K. Ågren, N. J. T. Edberg, and J. H. Waite Jr. (2013), Negative ion densities in the ionosphere of Titan–Cassini RPWS/LP results, *Planet. Space Sci.*, *84*, 153–162, doi:10.1016/j.pss.2013.05.021.
Smith, F. L., III, and C. Smith (1972), Numerical evaluations of Chapman's grazing incidence integral ch(X,x), *J. Phys. Res.*, *77*, 3592, doi:10.1029/JA077i019p03592.
Snowden, D., R. V. Yelle, M. Galand, A. J. Coates, A. Wellbrock, G. H. Jones, and P. Lavvas (2013), Auroral electron precipitation and flux tube erosion in Titan's upper atmosphere, *Icarus*, *226*(1), 186–204.
Solomon, S. C., P. B. Hays, and V. J. Abreu (1988), The auroral 6300 Å emission: Observations and modeling, *J. Geophys. Res.*, *93*, 9867–9882, doi:10.1029/JA093iA09p09867.
Tobiska, W. K. (2007), SOLAR 2000 v2.30 and SOLARFLARE v1.01: New capabilities for space system operations, *American Institute of Aeronautics and Astronautics, Inc.*
Tobiska, W. K., T. Woods, F. G. Eparvier, R. Viereck, L. Floyd, D. Bouwer, G. Rottman, and O. R. White (2000), The SOLAR2000 empirical solar irradiance model and forecast tool, *J. Atmos. Sol. Terr. Phys.*, *62*(14), 1233.
Ulusen, D., J. G. Luhmann, Y.-J. Ma, S. Ledvina, T. E. Cravens, K. Mandt, J. H. Waite, and J.-E. Wahlund (2010), Investigation of the force balance in the Titan ionosphere: Cassini T5 flyby model/data comparisons, *Icarus*, *210*, 867–880, doi:10.1016/j.icarus.2010.07.004.
Vigren, E., M. Hamberg, V. Zhaunerchyk, M. Kaminska, R. Thomas, M. Larsson, T. Millar, C. Walsh, and W. Geppert (2009), The dissociative recombination of protonated acrylonitrile and the upper atmosphere of Titan, *Astrophys. J.*, *695*, 317.
Vigren, E., et al. (2013), On the thermal electron balance in Titan's sunlit upper atmosphere, *Icarus*, *223*(2013), 234–251.
Vuitton, V., R. V. Yelle, and V. G. Anicich (2006), The nitrogen chemistry of Titan's upper atmosphere revealed, *Astrophys. J.*, *647*, L175–L178.
Vuitton, V., R. V. Yelle, and M. McEwan (2007), Ion chemistry and N-containing molecules in Titan's upper atmosphere, *Icarus*, *191*, 722–742.
Vuitton, V., R. Yelle, and J. Cui (2008), Formation and distribution of benzene on Titan, *J. Geophys. Res.*, *113*, E05007, doi:10.1029/2007JE002997.
Vuitton, V., P. Lavvas, R. V. Yelle, M. Galand, A. Wellbrock, G. R. Lewis, A. J. Coates, and J. E. Wahlund (2009), Negative ion chemistry in Titan's upper atmosphere, *Planet. Space Sci.*, *57*, 1558–1572, doi:10.1016/j.pss.2009.04.004.
Wahlund, J.-E., et al. (2005), Cassini measurements of cold plasma in the ionosphere of Titan, *Science*, *308*, 986–989.
Waite, J. H., et al. (2004), The Cassini Ion and Neutral Mass Spectrometer (INMS) investigation, *Space Sci. Rev.*, *114*(1), 113.
Waite, J. H., Jr., et al. (2005), Ion Neutral Mass Spectrometer (INMS) results from the first flyby of Titan, *Science*, *308*, 982–986.
Waite, J. H., Jr., D. T. Young, T. E. Cravens, A. J. Coates, F. J. Crary, B. Magee, and J. Westlake (2007), The process of tholin formation in Titan's upper atmosphere, *Science*, *316*, 870–875.
Watanabe, K., M. Zelikoff, and E. C. Y. Inn (1953), Absorption coefficients of several atmospheric gases, *Air Force Cambridge Research Centre Tech. Rep.* 52–53.
Westlake, J., J. Bell, J. Waite Jr, R. Johnson, J. Luhmann, K. Mandt, B. Magee, and A. Rymer (2011), Titan's thermospheric response to various plasma environments, *J. Geophys. Res.*, *116*, A03318, doi:10.1029/2010JA016251.
Westlake, J. H., J. H. Waite Jr., K. E. Mandt, N. Carrasco, J. M. Bell, B. A. Magee, and J.-E. Wahlund (2012), Titan's ionospheric composition and structure: Photochemical modeling of Cassini INMS data, *J. Geophys. Res.*, *117*, E01003, doi:10.1029/2011JE003883.
Wight, G. R., M. J. Van der Wiel, and C. E. Brion (1976), Dipole excitations, ionization and fragmentation of N_2 and CO in the 10–60 eV region, *J. Phys. B*, *9*, 675.
Wilson, E., and S. Atreya (2004), Current state of modeling the photochemistry of Titan's mutually dependent atmosphere and ionosphere, *J. Geophys. Res.*, *109*, E06002, doi:10.1029/2003JE002181.
Young, D. T., et al. (2005), Composition and dynamics of plasma in Saturn's magnetosphere, *Science*, *307*, 1262–1266.
Zabka, J., M. Polasek, D. Ascenzi, P. Tosi, and D. Schroder (2009), Reactivity of $C_2H_5^+$ with benzene: Formation of ethylbenzenium ions and implications for Titan's ionospheric chemistry, *J. Phys. Chem. A*, *113*(42), 11,153–11,160.